

The Density Profile of Dynamical Halos

Tristen Shields,* Edgar M. Salazar, Eduardo Rozo, and Aakanksha Adya
Department of Physics, University of Arizona, Tucson, AZ 85721, USA

Calvin Osinga and Ze'ev Vladimир
Department of Astronomy, University of Maryland, College Park, MD 20742, USA
(Dated: July 2, 2025)

Among the most fundamental properties of a dark matter halo is its density profile. Motivated by the recent proposal by García *et al.* [1] to define a *dynamical halo* as the collection of orbiting particles in a gravitationally bound structure, we characterize the mean and scatter of the orbiting profile of dynamical halos as a function of their orbiting mass. We demonstrate that the orbiting profile of individual halos at fixed mass depends on a single dynamical variable — the halo radius r_h — which characterizes the spatial extent of the profile. The scatter in halo radius at fixed orbiting mass is $\approx 16\%$. Only a small fraction of this scatter arises due to differences in halo formation time, with late-forming halos being more compact (smaller halo radii). Accounting for this additional correlation results in an $\approx 11\%$ scatter in halo radius at fixed mass and halo formation time.

I. INTRODUCTION

One of the most basic properties of a dark matter halo is its density profile. It is typically characterized by simple analytic expressions — e.g. the standard Navarro, Frenk, and White [2] or Einasto profiles [3] — which are fit to the total mass distribution in a halo interior to some reference radius, e.g. R_{200m} (the radius enclosing a mass equal to 200 times that of the mean matter density of the Universe). However, it is now broadly recognized that the dynamical structure of halos extends well past this radius. Today, the *splashback radius* [4–6] is broadly recognized as a more physically-motivated definition of the spatial extent of a halo [see also 7, 8]. Despite this, thinking of the splashback radius as a boundary is fundamentally incorrect: much of the mass on these scales is found within infall streams, and as such does not really belong to the halo yet. Indeed, these infall streams are dynamically distinct from the population of particles orbiting halos, and therefore should not be considered part of the halo.

Here, we adopt the halo definition proposed by García *et al.* [1], in which a halo is defined as the collection of orbiting particles around their self-generated potential. We follow Salazar *et al.* [9] in referring to halos defined in this way as *dynamical halos*. Our goal in this paper is to characterize the mean and scatter of the halo profile of dynamical halos. Our work is related to recent work by Diemer [10, 11], who characterized the orbiting profile of traditionally defined halos; and the work of Salazar *et al.* [9], who characterized the halo–mass correlation function of dynamical halos. While the two works differ on the precise parametric form used to describe the orbiting profile of halos, both of these works demonstrate the orbiting profile of halos is finite in spatial extent, with a slowly varying radial slope towards the halo center. We

have chosen to use the parameterization of Salazar *et al.* [9] as our fiducial parameterization because it has fewer free parameters than that of Diemer [11]. We comment on how this choice impacts our results in Section V.

Our paper is organized as follows: in Section II, we describe our simulation data set, and how the particles near halos are labeled as either orbiting or infalling. We also define an accretion time for each particle, which we will use later in the paper. In Section III, we describe the orbiting profile from Salazar *et al.* [9], and present our fits to the orbiting profiles of individual halos. We further demonstrate how the two parameters governing the halo profile are strongly correlated, enabling us to characterize individual halos profile using a single free parameter, the halo radius r_h . We also characterize the scatter in halo radius at fixed orbiting mass. In Section IV, we investigate how the halo radius correlated with a halo’s accretion history, and construct a model for the halo radius that incorporates our findings. In Section V, we compare our model to that of Diemer [11]. In Section VI we summarize our results and discuss their implications.

II. SIMULATION AND HALO CATALOG

This paper relies on the Cold Dark Matter (CDM) simulation described in [12]. This simulation was run using GADGET-2 [13] and uses a $1 h^{-1}$ Gpc box with 1024^3 particles. The simulation’s softening length is $15 h^{-1}$ kpc, and its cosmological parameters are $\Omega_m = 0.3$, $\Omega_\Lambda = 0.70$, $n_s = 0.96$, $h = 0.7$, $A_s = 2 \times 10^{-9}$, and $\sigma_s = 0.85$. The initial conditions are set at $z = 99$ using N-GenIC [14]. Here, we focus exclusively on halo density profiles at $z = 0$. To generate a dynamical halo catalog, we start with the catalog generated using the *Rockstar* halo finding algorithm [15]. Halo masses in the catalog are defined using a standard spherical overdensity definition with a threshold of 200 with respect to the mean.

With the *Rockstar* halo catalog in hand, we proceed to find the orbiting particles for every halo using the algo-

* tdshield@arizona.edu

rithm of García *et al.* [1]. Briefly, we start from the most massive **Rockstar** halo. Particles within $5 h^{-1}$ Mpc of the halo are tagged with the time at which the particle first crosses the scale associated with the one-to-two halo transition, defined as the minimum in $r^2 \xi_{\text{hm}}$ [1]. We refer to this time at the accretion time, which we denote a_{acc} . Particles with early accretion times and approximately zero time-averaged radial velocities are tagged as “orbiting,” while particles with late accretion times and negative time-averaged radial velocities are tagged as “in-falling.” The halo is then redefined as the collection of all orbiting particles and assigned an orbiting mass M_{orb} , the total mass of the orbiting particles. These orbiting particles are then removed from consideration when selecting orbiting particles for all subsequent halos, ensuring each particle orbits at most one halo. We then move on to the next largest halo, find its orbiting particles, and iterate until we run through the original halo catalog. The end result is a catalog of dynamical halos, with each halo having an associated list of orbiting particles.

Throughout this study, we will explore how halo properties depend on mass by binning halos in narrow mass bins. Specifically, all binned analyses below assume 9 halo mass bins with edges $\log(M_{\text{orb}}) \in [13.40, 13.55, 13.70, 13.85, 14.00, 14.15, 14.30, 14.45, 14.65, 15.00]$, where the orbiting mass M_{orb} is measured in $h^{-1} M_{\odot}$.

III. THE PROFILE OF DYNAMICAL HALOS

A. Parametric Fits

We describe the orbiting profile of dynamical halos using the parametric model of Salazar *et al.* [9], given by

$$\rho_{\text{orb}}(x|M_{\text{orb}}) = A \left(\frac{x}{\epsilon}\right)^{-\alpha(x|M_{\text{orb}})} \exp\left(-\frac{x^2}{2}\right). \quad (1)$$

Here, $x \equiv r/r_{\text{h}}$, where r_{h} is the length scale at which the exponential truncation of the orbiting profile “turns on.” Following Salazar *et al.* [9], we refer to this scale as the *halo radius*. A is a normalization constant chosen such that $\rho_{\text{orb}}(x)$ integrates to the halos orbiting mass, and as such is not a parameter in the model (we never fit for A). Lastly, ϵ is a mass-independent scaling parameter governing the run of the slope of the density profile α . Specifically, $\alpha(x)$ takes the functional form

$$\alpha(x|M_{\text{orb}}) = \alpha_{\infty} \frac{x}{x + \epsilon}. \quad (2)$$

Note the slope smoothly transitions from $\alpha = 0$ to $\alpha = \alpha_{\infty}$ at scales $r \gg \epsilon r_{\text{h}}$. The model has a total of three parameters: r_{h} , α_{∞} , and ϵ . We follow Salazar *et al.* [9] in setting $\epsilon = 0.037$, leaving only two free parameters with which to fit the orbiting profile of dynamical halos. Salazar *et al.* [9] fit the *stacked* density profile of dynamical halos, finding both α_{∞} and r_{h} vary with mass as

Table I. Maximum likelihood parameter values from Salazar *et al.* [9] from Equations (1)-(4).

Parameter	Description	Value
$r_{\text{h,p}}$	Halo radius pivot (kpc h^{-1})	840.3 ± 2.2
$r_{\text{h,s}}$	Halo radius power	0.226 ± 0.003
$\alpha_{\infty,p}$	Asymptotic slope pivot	2.018 ± 0.002
$\alpha_{\infty,s}$	Asymptotic slope power	-0.050 ± 0.001
ϵ	Inner scaling	0.037 ± 0.001
M_{p}	Pivot mass	$10^{14} M_{\odot}$

power-laws,

$$r_{\text{h,st}}(M_{\text{orb}}) = r_{\text{h,p}} \left(\frac{M_{\text{orb}}}{M_{\text{p}}}\right)^{r_{\text{h,s}}}, \quad (3)$$

$$\alpha_{\infty,\text{st}}(M_{\text{orb}}) = \alpha_{\infty,p} \left(\frac{M_{\text{orb}}}{M_{\text{p}}}\right)^{\alpha_{\infty,s}}. \quad (4)$$

The subscripts ‘p’ and ‘s’ denote the pivots and slopes, respectively, while the subscript ‘st’ indicates that these parameters are measured using halo stacks of fixed mass. The pivot mass is $M_{\text{p}} = 10^{14} h^{-1} M_{\odot}$. As expected, as halos become more massive they also become more extended and less concentrated (i.e. α_{∞} decreases). Table I summarizes the best fit values for these parameters as reported in Salazar *et al.* [9].

The left panel in Figure 1 shows the orbiting density profiles for 100 random halos in three different mass bins, as labeled. Also shown as black solid curves are the best fit parametric model of Salazar *et al.* [9] to the *stacked* orbiting profile. Motivated by the excellent agreement between the model stacked profile and the individual orbiting profiles, we proceed to fit each individual halo with Equation (1). When doing so, we do not include points within the gray shaded area, corresponding to radii smaller than six times the softening length. We adopt a cost function in which the error term is the sum in quadrature of a Poisson uncertainty in the number of particles at any given radius, and a fixed per-cent error in the number of particles. This results in the cost function

$$\chi^2 = \sum_i \frac{(N_{\text{data},i} - N_{\text{orb}}(r_i))^2}{(\delta N_{\text{data},i})^2 + N_{\text{data},i} + 1}. \quad (5)$$

Here, N_{orb} is the number of orbiting particles predicted at any given radius, and $\delta = 0.05$, corresponding to a 5% error in the counts. We have verified our results are only marginally sensitive to the precise value of δ chosen. Finally, we add a “+1” term in the variance to ensure the variance is non-zero when $N_{\text{data}} = 0$. With this cost function in hand, we find the best fit halo radius r_{h} and slope α_{∞} for every halo in the catalog.

To illustrate the quality of our fits, for each halo we calculated the scaled density profile $\tilde{\rho}_{\text{orb}}$ defined via

$$\tilde{\rho}_{\text{orb}}(x) \equiv \frac{1}{A} \left(\frac{x}{\epsilon}\right)^{\alpha(x)} \rho_{\text{orb}}(x). \quad (6)$$

In the above Equation, ρ_{orb} is the density profile measured in the data as a function of the scaled radius r/r_{h} .

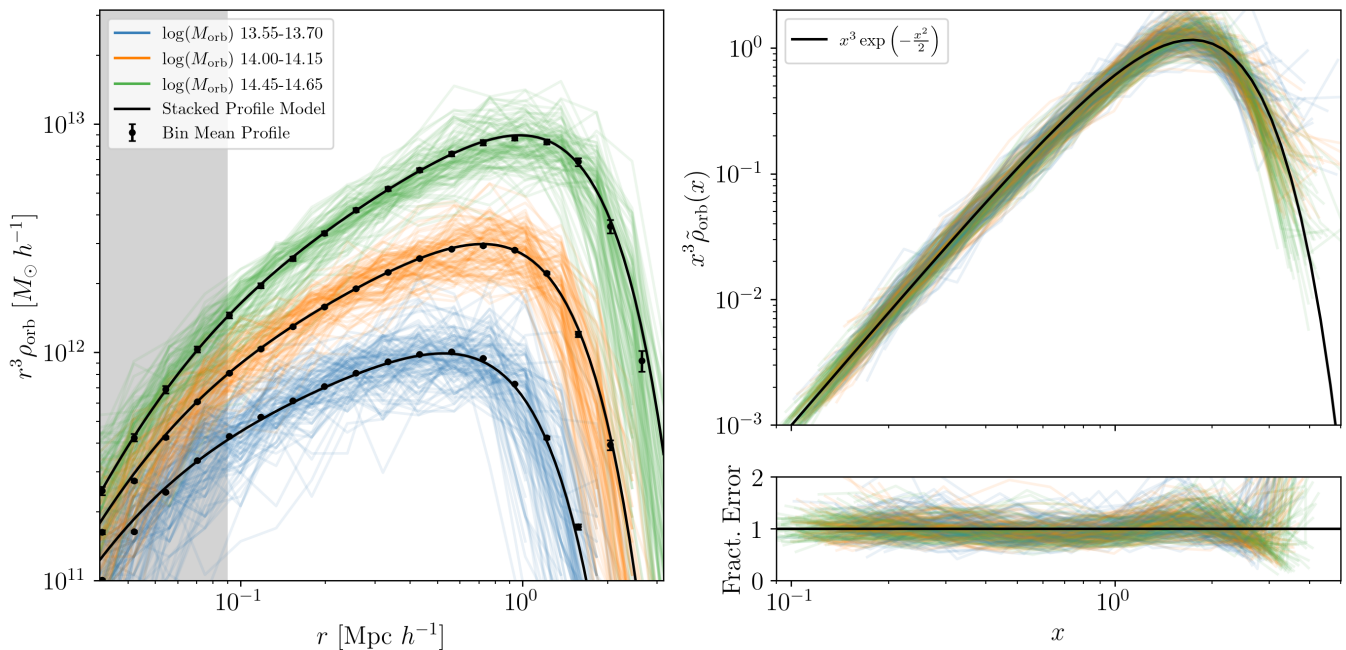


Figure 1. **Left:** Orbiting density profiles ($r^3 \rho_{\text{orb}}$ vs. r) of 300 random halos in three mass bins as labeled. Each mass bin has 100 randomly selected halos. Also shown as points with error bars are the mean orbiting profiles from all halos in the bin. The solid black lines are the best fit model obtained using Equation 1. Scales $r \leq 0.09 h^{-1} \text{ Mpc}$ (gray band) are subject to force-softening, and are therefore not fit. **Top-Right:** Scaled density profiles $x^3 \tilde{\rho}_{\text{orb}}$ (see Equation (6)) of the same 300 halos shown at left, as a function of $x \equiv r/r_h$, where r_h is the best-fit halo radius for each individual halo. The black solid line is the expectation for the rescaled profiles, $x^3 \exp(-x^2/2)$. **Bottom-Right:** Fractional error between the profiles from individual halos and each halo’s own best fit model.

When scaled in this way, the resulting orbiting profile is expected to be independent of halo mass, with

$$\tilde{\rho}_{\text{orb}}(x) = \exp(-\frac{1}{2}x^2). \quad (7)$$

The right panel in Figure 1 compares the scaled density profile $\tilde{\rho}_{\text{orb}}$ for the same 300 halos shown in the left panel. The solid black line is the corresponding expectation $\tilde{\rho}_{\text{orb}} = \exp(-\frac{1}{2}x^2)$ (note we actually plot $x^3 \tilde{\rho}_{\text{orb}}$). The bottom-right panel corresponds to the relative difference between the scaled profiles and our model expectation. As we can see, the residuals are consistent with zero within noise.

B. On the Degrees of Freedom of Orbiting Profiles

Having fit every halo with Equation (1), we wish to characterize how halos can vary in spatial extent (r_h) and slope (α_{∞}) at fixed mass. To that end, we first isolate how the profile of an individual halo differs from the corresponding stacked profile by defining

$$\Delta\alpha_{\infty} \equiv \alpha_{\infty} - \alpha_{\infty,\text{st}}(M_{\text{orb}}) \quad (8)$$

$$R \equiv \frac{r_h}{r_{h,\text{st}}(M_{\text{orb}})} \quad (9)$$

where $r_{h,\text{st}}(M_{\text{orb}})$ and $\alpha_{\infty,\text{st}}(M_{\text{orb}})$ are the stacked halo radius and slope given by Equations 3 and 4.

In Figure 2 we show how simulated halos populate the $\Delta\alpha_{\infty}-R$ space. Evidently, the two parameters are strongly correlated, so that at fixed mass, more extended halos (higher r_h) having steeper inner slopes. The red line is obtained by maximizing a cost function given by the number of haloes with a $\Delta\alpha_{\infty}$ of ± 0.03 of the line. The resulting best-fit line is given by

$$\Delta\alpha_{\infty} = (0.049 \pm 0.002) + (1.002 \pm 0.021) \ln R \quad (10)$$

where the error bars come from Jackknifing the box. In light of these values, we have opted to adopt

$$\Delta\alpha_{\infty} = 0.05 + \ln R \quad (11)$$

as our fiducial model. From these results it is clear that while our parametric fits contains two free parameters, the tight correlation between α_{∞} and r_h implies that halo profiles have a single effective degree of freedom, namely the halo radius r_h . In particular, a halo of mass M_{orb} and radius r_h has a density slope

$$\alpha_{\infty} = \alpha_{\infty,\text{st}}(M_{\text{orb}}) + \ln[r_h/r_{h,\text{st}}(M_{\text{orb}})] + 0.05. \quad (12)$$

C. The Distribution of Halo Radii at Fixed Mass

In light of the above results, we have refit every halo using the halo radius as the only free parameter

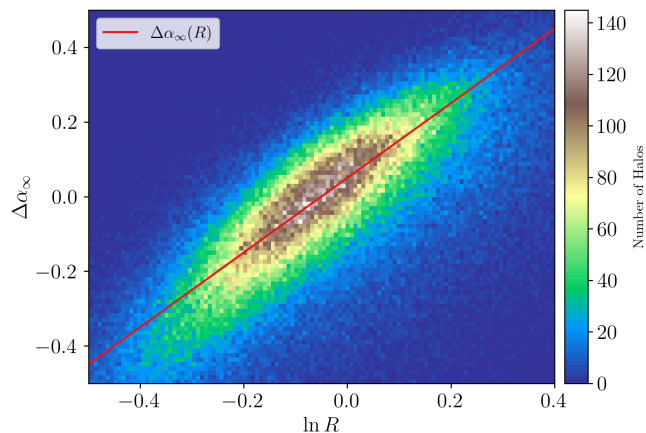


Figure 2. The color scale shows the number of dark matter halos in each pixel in the space of slope offset $\Delta\alpha_\infty$ (Equation 8) and rescaled halo radius (Equation 9). We see the inner slope of a halo is tightly correlated with the scaled halo radius, a correlation we summarized by our best-fit line shown in red.

in the model, with the slope $\alpha_\infty(r_h, M_{\text{orb}})$ set as per Equation (12). The quality of the fits is very similar to that illustrated in Figure 1, and is therefore not shown. Figure 3 shows that the distribution of \log -radii $\ln r_h/r_{h,\text{st}}(M_{\text{orb}})$ in bins of mass is approximately Gaussian. All distributions peak at the same ratio

$$\frac{r_h}{r_{h,\text{st}}} = 0.937, \quad (13)$$

with the width of the distributions increasing with decreasing mass. We attribute this mass dependence to increasing measurement uncertainties as the number of particles in a halo decreases. Indeed, we find that we can accurately describe the mass dependence of the variance using a fit of the form

$$\text{Var}(\ln r_h/r_{h,\text{st}}|N) = \sigma_0^2 + \frac{k}{N} \quad (14)$$

where N is the number of orbiting particles in a halo of mass M_{orb} . We adopt our best fit value $\sigma_{\ln r_h/r_{h,\text{st}}|M_{\text{orb}}} = 0.16$ as our best fit value for the scatter in r_h at fixed mass.

IV. DEPENDENCE OF THE HALO RADIUS ON ACCRETION HISTORY

It has long been known that the structure of a halo is correlated with its formation history [e.g. 16]. We wish to test the extent to which the orbiting profile of a halo can be predicted using its accretion history, as characterized by the distribution of accretion times a_{acc} of the orbiting particles in a halo. To that end, we look for differences in the distribution of particle accretion times for extended (large r_h) and compact (small r_h) halos at fixed mass. Figure 4 shows the Cumulative Distribution Functions

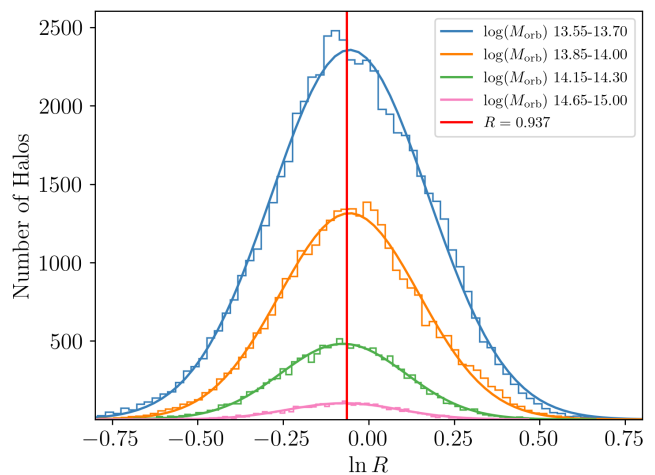


Figure 3. The distribution of $\ln r_h/r_{h,\text{st}}$ in bins of fixed mass. We see that the halo radius r_h is roughly lognormally distributed, with an average value $\langle \ln r_h/r_{h,\text{st}}|M_{\text{orb}} \rangle = \ln 0.937 = -0.064$. After accounting for particle noise, the intrinsic scatter in $\ln r_h/r_{h,\text{st}}$ at fixed mass is $\sigma_{\ln r_h/r_{h,\text{st}}|M_{\text{orb}}} = 0.16$.

(CDF) of particle accretion times (a_{acc}) for halos split by the scaled halo radius $R \equiv r_h/r_{h,\text{st}}$. Each mass bin is split into six logarithmically spaced R bins, with each bin being one standard deviation in $\ln R$ wide. Because a_{acc} was measured only up to $a = 0.4$, particles with earlier accretion times are assigned an accretion time of $a_{\text{acc}} = 0.4$. This means our CDFs are correct for $a_{\text{acc}} > 0.4$, but are unresolved below this threshold.

The fact that massive halos form at late times leads to a systematic rightwards shift in the CDF for a_{acc} as one moves towards more massive halos. Of more interest to us, however, is how the CDF of halos depend on r_h at fixed halo mass. It is obvious from Figure 4 that halos with different halo radii also have different accretion histories: the most compact halos form at late times, while the most extended halos form at early times.

To quantify the differences in accretion history for halos of different halo radii, we wish to define a parameter that cleanly separates the different CDF curves within each mass bin. Upon inspection, we define a_{60} as the value of a_{acc} at which the CDF reaches

$$\text{CDF}(a_{60}) = 0.60 \quad (15)$$

and use it to differentiate early halos from late forming halos. Unfortunately, the fact that more massive halos form later implies that a_{60} correlates with halo mass. This is undesirable for the purposes of characterizing *relative* differences in formation. Consequently, we define the *relative formation time* variable a_{RF} via

$$a_{\text{RF}} \equiv \frac{a_{60}}{\text{median}(a_{60}|M_{\text{orb}})}. \quad (16)$$

Note that since the earliest particle accretion time in our dataset is $a_{\text{acc}} = 0.4$, the relative formation time of halos

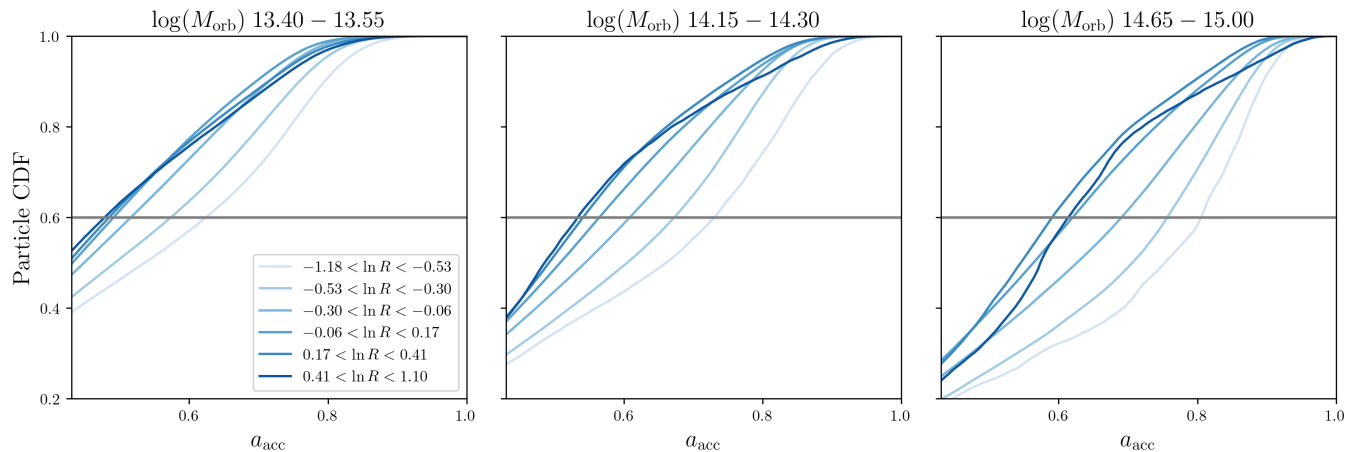


Figure 4. After binning all of the halos by M_{orb} , then binning again by $\ln R$, we take CDFs of the particle accretion times of all the particles belonging to halos in those bins. A horizontal line is drawn when the CDF reaches 0.6, as at this point there is visually a clear distinction between most of the $\ln R$ bins that is approximately constant with mass.

with $a_{60} < 0.4$ is not resolved. For this reason, for the remainder of this analysis we focus exclusively on halos with $M_{\text{orb}} > 10^{14} h^{-1} M_{\odot}$. At these high masses, nearly all ($> 99\%$) halos have $a_{60} > 0.4$.

In the left panel of Figure 5 we plot the relative formation time of every massive ($M_{\text{orb}} \geq 10^{14} h^{-1} M_{\odot}$) halo against its corresponding halo radius. The two are clearly correlated, with

$$R = a_0 + s_a a_{\text{RF}} \quad (17)$$

where $a_0 = 1.89 \pm 0.03$ and $s_a = -0.98 \pm 0.02$. Errors come from jackknifing the box. In light of this result, we adopt a model with $s_a = -1.0$, with a corresponding best fit value $a_0 = 1.91 \pm 0.01$. Thus, our expression for the halo radius takes the form

$$r_{\text{h,mod}}(a_{\text{RF}}, M_{\text{orb}}) = (1.91 - a_{\text{RF}}) r_{\text{h,st}}(M_{\text{orb}}) \quad (18)$$

where the subscript ‘mod’ starts for “model.”

Note massive halos with small halo radii both form later and have shallower profiles, consistent with the usual relation that late forming halos are less concentrated [16].

Unfortunately, the relation between halo formation time and halo radius in Figure 5 is noisy. Consequently, there remains significant scatter in the distribution of halo radius at fixed mass and halo formation time. In particular, as in Section III C, we find the distribution of

$$\tilde{R} \equiv \frac{r_{\text{h}}}{r_{\text{h,mod}}(M_{\text{orb}}, a_{\text{RF}})} \quad (19)$$

is lognormally distributed with $\langle \ln \tilde{R} | M_{\text{orb}} \rangle = 0.018 \pm 0.003$, independent of mass. As in Section III C, the scatter is mass dependent due to particle noise; the best fit intrinsic scatter in r_{h} at fixed mass and halo formation time is $\sigma_{\ln r_{\text{h}} | M_{\text{orb}}, a_{\text{RF}}} = 0.11$. This is down from the 0.16 scatter in radius at fixed mass in the absence

of any information about a halo’s formation time, but only marginally so. Evidently, differences in the relative formation time parameter are insufficient to explain the scatter in halo radius at fixed mass. For reference, we can also consider the best fit halo radius r_{h} obtained when fitting the density profiles with α_{∞} as a free parameter, and then using Figure 6 to predict r_{h} as a function of M_{orb} and α_{∞} . When we do so, the distribution of halo radii has a core with a scatter of only $\approx 5\%$, though large non-gaussian tails appear. That is, relative to the predictions based on relative formation time, there is significant room for improvement with regards to our ability to predict r_{h} from halo properties.

Before moving on, we test whether our results on halo radii are internally self-consistent. Specifically, we have found both that

$$\langle \ln r_{\text{h}} / r_{\text{h,mod}} | M_{\text{orb}}, a_{\text{RF}} \rangle = 0.018 \quad (20)$$

and

$$\langle \ln r_{\text{h}} / r_{\text{h,st}} | M_{\text{orb}} \rangle = -0.064. \quad (21)$$

These two values must be related to each other. Multiplying Equation 20 by $P(a_{\text{RF}} | M_{\text{orb}})$ and integrating, we find after some algebra that

$$\langle \ln(r_{\text{h}} / r_{\text{h,st}}) | M_{\text{orb}} \rangle = 0.018 + \langle \ln(1.91 - a_{\text{RF}}) | M_{\text{orb}} \rangle. \quad (22)$$

Evaluating the right hand side of the above Equation by averaging over the distribution of relative formation times we obtain $\langle \ln(r_{\text{h}} / r_{\text{h,st}}) | M_{\text{orb}} \rangle = -0.094$. This value differs from our best fit by 0.029. We attribute this 3% difference to the impact of non-Gaussian tails in the distribution of halo radii.

V. COMPARISON TO DIEMER 2025

Diemer [17] recently published an analysis similar to

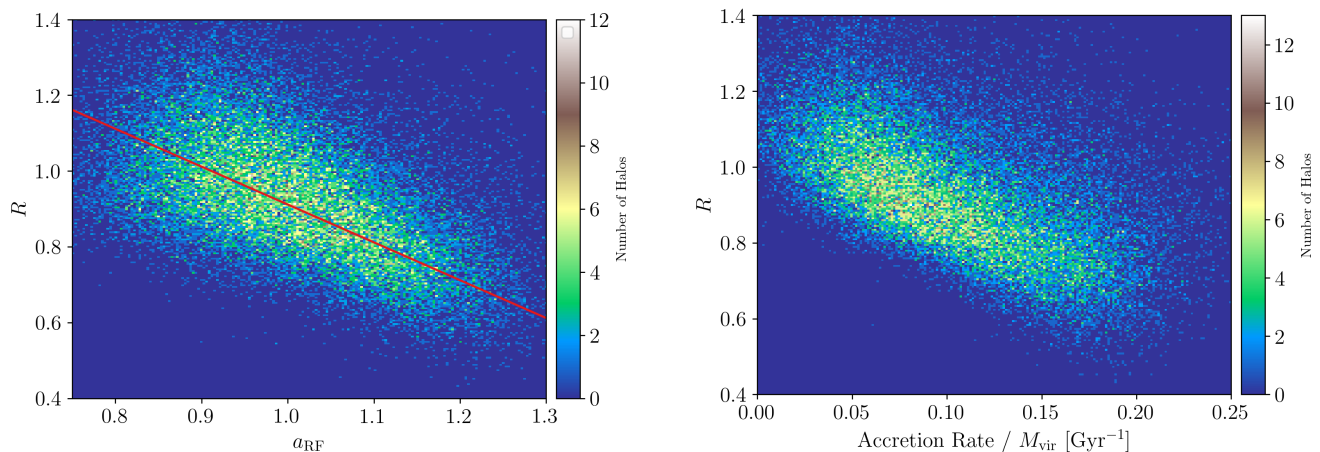


Figure 5. **Left:** Correlation between the normalized halo radius (Equation 9) and a halo’s relative formation time (Equation 16) at fixed mass, for halos of mass $M_{\text{orb}} > 10^{14} h^{-1} M_{\odot}$. Our best fit line for this correlation is shown in red. **Right:** Correlation between halo radius at fixed halo mass, as a function of halo accretion rate divided by halo virial mass. The qualitative trends is similar to that of the left panel, though the relation with accretion rate exhibits larger tails.

ours. However, the two works differ in that:

1. Diemer focuses on the properties of ρ_{orb} for spherical overdensity halos, whereas we focus specifically on dynamical halos. Even though the difference in algorithms has a minimal impact on the orbiting profiles of individual halos [18], the choice of definition matters with regards to the scatter and correlation of halo properties with mass.
2. Diemer relies on the parametric model of Diemer [11], which takes the form

$$\rho_{\text{orb}}(r) = \rho_s \exp(S(r)) \quad (23)$$

where

$$S(r) \equiv -\frac{2}{\alpha} \left[\left(\frac{r}{r_s} \right)^{\alpha} - 1 \right] - \frac{1}{\beta} \left[\left(\frac{r}{r_t} \right)^{\beta} - \left(\frac{r_s}{r_t} \right)^{\beta} \right] \quad (24)$$

We note that while the Diemer model has four degrees of freedom (r_t , r_s , α , and β), when fitting individual halo profiles Diemer holds the parameters α and β fixed to their best-fit values in the stacked profile, $\alpha = 0.18$ and $\beta = 3.0$. This reduces the number of degrees of freedom in the individual fits to two, the same number of degrees of freedom in the Salazar *et al.* [9] (r_h and α_{∞}). However, this reduction in parameter space is not unique, a point that we return to below. For now, we simply note that when fitting individual halo profiles, Diemer varies only the radius r_t and the scale radius r_s : the radius r_t is roughly equivalent to the halo radius r_h in Salazar *et al.* [9], while the scale radius r_s is roughly equivalent to α_{∞} , as they both characterize the slope of the density profile in the core of the halo. With this understanding in hand, we show below that the two works are in agreement with regards to the qualitative trends in the profiles. Unfortunately, quantitative comparisons are non-trivial because the two works adopt different halo mass definitions.

We begin by considering how the extent of the orbiting profile correlates with mass. Diemer [17] finds the ratio r_t/R_{200m} decreases with increasing mass, implying the slope of r_t with M_{200m} is smaller than $1/3$. Since $M_{200m} \approx M_{\text{orb}}$ [Fig. 9 in 1], this is consistent with the $\approx 1/4$ power-law index in the relation between r_h and M_{orb} in Salazar *et al.* [9]. That is, *the spatial extent of orbiting halos scales with mass with a power-law index flatter than $1/3$.*

We then turn to the tight correlation between α_{∞} and r_h obtained from fitting individual halos (see Figure 2). This correlation is also apparent in the correlation between r_s and r_t in Figure 10 of Diemer [17]: in units of R_{200m} , halos with larger r_t have a smaller r_s , resulting in steeper inner profiles, precisely as per Figure 2. However, the correlation in our Figure 2 appears to have smaller scatter than the one shown in Figure 10 of Diemer [17]. We attribute the increased scatter in the latter work to two factors: 1) when fitting individual halo profiles, Diemer [17] set $\alpha = 0.18$ and $\beta = 3$, rather than solving for the relations $\alpha(r_t)$ and $\beta(\alpha)$ apparent in their Figure 3. That is, the reduction in parameters space in Diemer [17] was sub-optimal, leading to increased scatter. Second, while Figure 10 of Diemer [17] roughly accounts for the mass dependence of r_s and r_t , neither of these length scales is exactly proportional to R_{200m} . Consequently, some of the scatter in Figure 10 of Diemer [17] is due to trends of r_s/R_{200m} and r_t/R_{200m} with mass. Despite these differences, the main conclusion is the same: *at fixed mass, the more extended a halo is, the steeper its inner density profile is.*

At this point, the comparison between our results and those of Diemer [17] becomes more difficult. Based on the tight correlation between α_{∞} and r_h , we adopted r_h as the single free parameter in our model. By contrast, Diemer [17] maintained both r_s and r_t as free param-

ters, albeit with significant scatter. Nevertheless, we find similar qualitative trends. Diemer [17] finds that while r_t does not vary strongly with halo formation time, r_s does: early forming halos have lower r_s/R_{200m} values, resulting in steeper profiles. These early halos must therefore have large α_∞ values, which in turn correspond to large halo radii, i.e. *early forming halos have larger radii*, in agreement with our results (see Figure 5).

We have further shown that there remains significant scatter in the distribution of halo radii r_h at fixed halo mass, even after accounting for the impact of the relative formation time parameter a_{RF} on r_h . Based on the self-similar collapse model, the splashback radius is expected to depend primarily not on halo mass, but rather on accretion rate [19–21]. Indeed, Diemer [17] finds that their radial boundary r_t is tightly correlated with a halo’s recent accretion rate Γ (see their Figure 12), where Γ is the average halo mass accretion rate ($\Gamma \equiv \Delta \ln M_{200m} / \Delta \ln a$) over one dynamical time (see [17] for details). Similar conclusions hold for the splashback radius in simulations Shin and Diemer [22].

The right panel in Figure 5 shows that the variation in halo radius at fixed halo mass (i.e. $R \equiv r_h / r_{h,\text{st}}$) is correlated with accretion rate per unit mass as measured using the `Acc_Rate_2Tdyn` tag from `CONSTISTENT TREES` [23]. This accretion rate is the change in spherical overdensity mass of halo over a dynamical time $t_{\text{dyn}} = 2R_{200}/v_{200}$, divided by the present day mass. Note this definition is similar — but not identical — to that used in Diemer [17]. Comparing the left panel in Figure 5 to the right panel, we see that the correlation between halo radius and relative formation time is comparable to that between halo radius and accretion rate. In particular, although the latter appears to be slightly tighter, it also has more pronounced tails. Overall, we do not see a clear preference for selecting accretion rate over relative formation time as the relevant dynamical variable that controls variations in halo radii at fixed halo mass. However, we caution that we have not been able to self-consistently estimate halo accretion rates for dynamical halos, an omission we intend to address with the ability to quickly generate dynamical halo catalogs (Salazar et al., in preparation).

VI. SUMMARY AND IMPLICATIONS

In this work, we sought to characterize the density profile of dynamical halos. Our main results are:

- The individual orbiting density profiles of dynamical halos can be adequately fit using the $\rho_{\text{orb}}(r)$ parametric model of Salazar *et al.* [9], which contains two free parameters: a logarithmic slope α_∞ , and a parameter r_h , the exponential decay length governing the finite spatial extent of the orbiting profile. We refer to r_h as the *halo radius*.
- At fixed orbiting mass, the slope of the profile (α_∞) is tightly correlated with halo mass, with more ex-

tended halos having steeper slopes. This allows us to reduce the number of free parameters in the $\rho_{\text{orb}}(r)$ model to *one*: the halo radius.

- At fixed mass, the halo radius is correlated with halo formation time, such that at fixed mass, halos with early forming halos having more extended profiles with steeper slopes.
- The intrinsic scatter in halo radius at fixed mass is $\sigma_{\ln r_h | M_{\text{orb}}} = 0.16$. Accounting for the correlation between halo formation time and halo radius, we are able to reduce the scatter in halo radius to $\sigma_{\ln r_h | M_{\text{orb}}, a_{\text{RF}}} = 0.11$. The trends of halo radius with relative formation time are qualitative similar to those between halo radius and accretion rate.

This work is intimately related to that recently published by Diemer [17], who characterized the orbiting profiles of spherical halos using the parametric model advocated for in [11]. While these differences make quantitative comparisons of our results difficult, we argue either model constitutes an effective parameterization of the same underlying phenomenology. We refer the reader to Section V for a more comprehensive discussion of how the two works are related.

An interesting implications of our results is that if one is able to determine the structural properties of a halo, namely its halo radius and slope α_∞ , then one can recover both the mass and formation time of the halo. This is illustrated in Figure 6, where we plot the distribution of halos in the (r_h, a_{RF}) -plane, color coded by either mass (left panel) or relative formation time (right panel). The red solid lines are contours of fixed mass (left panel) or relative formation time (right panel) calculated using Equations 18 and 11. Evidently, one can “read off” the mass and formation time of a halo from its radius and slope, albeit with significant scatter.

DATA AVAILABILITY

All simulation data is available upon request. The code used to perform this analysis is publicly available on GitHub at https://github.com/tristen-shields/dark_matter_halo_profiles2025.

ACKNOWLEDGEMENTS

T.S. was supported in part through the Arizona NASA Space Grant Consortium, Cooperative Agreement 80NSSC20M0041. E.R. and E.S. were supported by NSF grant 2206688, and DOE grant DE-SC0009913. This research was supported in part by the National Science Foundation under Grant number 2206690. Participation of A.A. in this research was supported by the University of Arizona TIMESTEP program through the TIMESTEP Research Apprenticeship Program. E.R.

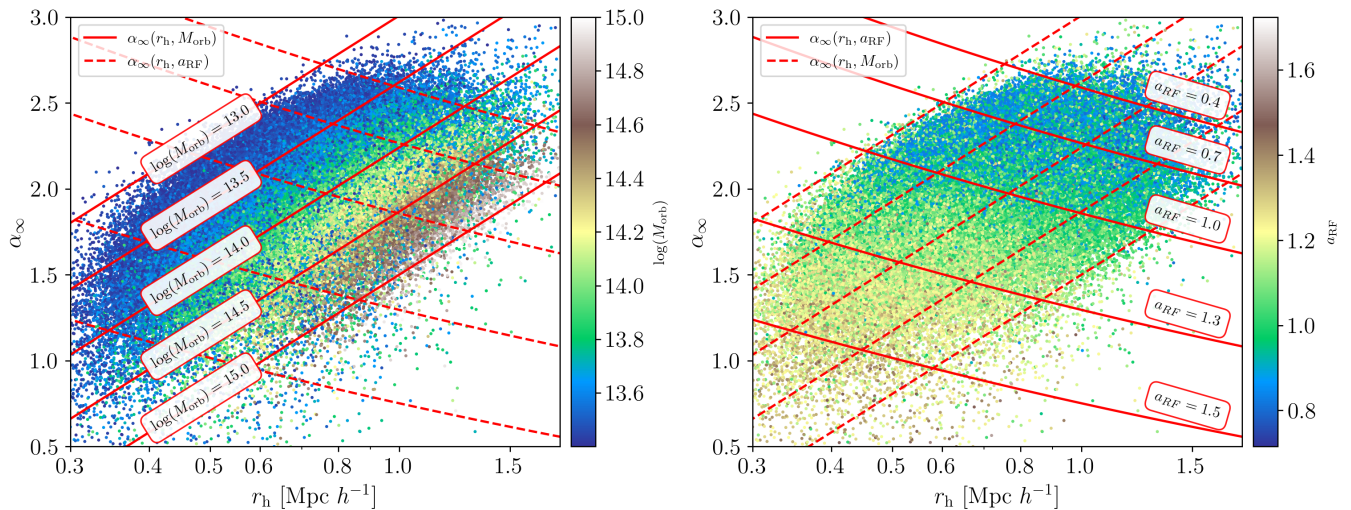


Figure 6. Visual representation of the relationships between r_h , α_∞ , M_{orb} , and a_{RF} . Both panels show how halos populate the space of halo radius r_h and slope α_∞ . In the left plot, halos are color-coded by mass, while on the right they are color coded by relative formation time. The solid red lines in the left plot show contours of fixed mass in Equation 11, as labeled. Changing a_{RF} moves a halo along these lines. The solid lines in the right hand show contours of a_{RF} as labeled. The solid lines on the left panel are shown as dotted lines on the right panel, and vice versa. Varying mass at fixed relative formation time moves halos along these lines.

gratefully acknowledges productive conversations with

Andrew Zentner and Susmita Adhikari.

-
- [1] R. García, E. Salazar, E. Rozo, S. Adhikari, H. Aung, B. Diemer, D. Nagai, and B. Wolfe, A better way to define dark matter haloes, *MNRAS* **521**, 2464 (2023), arXiv:2207.11827 [astro-ph.CO].
- [2] J. F. Navarro, C. S. Frenk, and S. D. M. White, A Universal Density Profile from Hierarchical Clustering, *Astrophys. J.* **490**, 493 (1997), arXiv:astro-ph/9611107 [astro-ph].
- [3] J. Einasto, On the Construction of a Composite Model for the Galaxy and on the Determination of the System of Galactic Parameters, *Trudy Astrofizicheskogo Instituta Alma-Ata* **5**, 87 (1965).
- [4] B. Diemer and A. V. Kravtsov, Dependence of the Outer Density Profiles of Halos on Their Mass Accretion Rate, *Astrophys. J.* **789**, 1 (2014), arXiv:1401.1216 [astro-ph.CO].
- [5] S. More, B. Diemer, and A. V. Kravtsov, The Splashback-jacob.d.santiago2.mil@us.navy.mil Radius as a Physical Halo Boundary and the Growth of Halo Mass, *Astrophys. J.* **810**, 36 (2015), arXiv:1504.05591 [astro-ph.CO].
- [6] P. Mansfield, A. V. Kravtsov, and B. Diemer, Splashback Shells of Cold Dark Matter Halos, *Astrophys. J.* **841**, 34 (2017), arXiv:1612.01531 [astro-ph.CO].
- [7] R. García, E. Rozo, M. R. Becker, and S. More, A redefinition of the halo boundary leads to a simple yet accurate halo model of large-scale structure, *MNRAS* **505**, 1195 (2021), arXiv:2006.12751 [astro-ph.CO].
- [8] M. Fong and J. Han, A natural boundary of dark matter haloes revealed around the minimum bias and maximum infall locations, *MNRAS* **503**, 4250 (2021), arXiv:2008.03477 [astro-ph.CO].
- [9] E. M. Salazar, E. Rozo, R. García, N. Kokron, S. Adhikari, B. Diemer, and C. Osinga, Dynamics-based halo model for large scale structure, *Phys. Rev. D* **111**, 043527 (2025), arXiv:2406.04054 [astro-ph.CO].
- [10] B. Diemer, A dynamics-based density profile for dark haloes - I. Algorithm and basic results, *MNRAS* **513**, 573 (2022), arXiv:2112.03921 [astro-ph.CO].
- [11] B. Diemer, A dynamics-based density profile for dark haloes - II. Fitting function, *MNRAS* **519**, 3292 (2023), arXiv:2205.03420 [astro-ph.CO].
- [12] F. Villaescusa-Navarro, C. Hahn, E. Massara, A. Banerjee, A. M. Delgado, D. K. Ramanah, T. Charnock, E. Giusarma, Y. Li, E. Allys, A. Brochard, C. Uhlemann, C.-T. Chiang, S. He, A. Pisani, A. Obuljen, Y. Feng, E. Castorina, G. Contardo, C. D. Kreisch, A. Nicola, J. Alsing, R. Scoccimarro, L. Verde, M. Viel, S. Ho, S. Mallat, B. Wandelt, and D. N. Spergel, The Quijote Simulations, *ApJS* **250**, 2 (2020), arXiv:1909.05273 [astro-ph.CO].
- [13] V. Springel, The cosmological simulation code GADGET-2, *MNRAS* **364**, 1105 (2005), arXiv:astro-ph/0505010 [astro-ph].
- [14] V. Springel, N-GenIC: Cosmological structure initial conditions, Astrophysics Source Code Library, record ascl:1502.003 (2015).
- [15] P. S. Behroozi, R. H. Wechsler, and H.-Y. Wu, The ROCKSTAR Phase-space Temporal Halo Finder and the Velocity Offsets of Cluster Cores, *Astrophys. J.* **762**, 109 (2013), arXiv:1110.4372 [astro-ph.CO].

- [16] R. H. Wechsler, J. S. Bullock, J. R. Primack, A. V. Kravtsov, and A. Dekel, Concentrations of Dark Halos from Their Assembly Histories, *Astrophys. J.* **568**, 52 (2002), arXiv:astro-ph/0108151 [astro-ph].
- [17] B. Diemer, A dynamics-based density profile for dark haloes - III. Parameter space, *MNRAS* **536**, 1718 (2025), arXiv:2410.17324 [astro-ph.CO].
- [18] Z. Vladimir, C. Osinga, B. Diemer, E. M. Salazar, and E. Rozo, Distinguishing Orbiting and Infalling Dark Matter Particles with Machine Learning, arXiv e-prints , arXiv:2506.09146 (2025), arXiv:2506.09146 [astro-ph.CO].
- [19] E. Bertschinger, Self-similar secondary infall and accretion in an Einstein-de Sitter universe, *ApJS* **58**, 39 (1985).
- [20] J. A. Fillmore and P. Goldreich, Self-similar gravitational collapse in an expanding universe, *Astrophys. J.* **281**, 1 (1984).
- [21] X. Shi, The outer profile of dark matter haloes: an analytical approach, *MNRAS* **459**, 3711 (2016), arXiv:1603.01742 [astro-ph.CO].
- [22] T.-h. Shin and B. Diemer, What sets the splashback radius of dark matter haloes: accretion history or other properties?, *MNRAS* **521**, 5570 (2023), arXiv:2210.14262 [astro-ph.CO].
- [23] P. S. Behroozi, R. H. Wechsler, H.-Y. Wu, M. T. Busha, A. A. Klypin, and J. R. Primack, Gravitationally Consistent Halo Catalogs and Merger Trees for Precision Cosmology, *Astrophys. J.* **763**, 18 (2013), arXiv:1110.4370 [astro-ph.CO].